energy&fuels

ACS EDITORS' CHOICE

pubs.acs.org/EF

Article

Probing Aggregation Tendencies in Asphaltenes by Gel Permeation Chromatography. Part 2: Online Detection by Fourier Transform Ion Cyclotron Resonance Mass Spectrometry and Inductively Coupled Plasma Mass Spectrometry

Jonathan C. Putman, Rémi Moulian, Donald F. Smith, Chad R. Weisbrod, Martha L. Chacón-Patiño, Yuri E. Corilo, Greg T. Blakney, Leah E. Rumancik, Caroline Barrère-Mangote, Ryan P. Rodgers, Pierre Giusti, Alan G. Marshall,* and Brice Bouyssière*

Cite This: *Energy Fuels* 2020, 34, 10915−10925

Read Online

ACCESS | Metrics & More | Article Recommendations

ABSTRACT: This work is the second installment of a study that probes the aggregation behavior of asphaltenes by gel permeation chromatography (GPC). In part 1, analysis of GPC aggregate fractions collected from the 2017 PetroPhase asphaltene sample by direct infusion revealed an inverse correlation between aggregate size and aromaticity. However, characterization of the largest aggregate fractions by direct infusion was hampered by solvent contaminant peaks and dynamic range limitations due to the extremely low ionization efficiencies of the larger, more aliphatic species that comprise those fractions. Here, we couple the GPC separation with online detection by positive atmospheric pressure photoionization ((+)APPI) 21 T Fourier transform ion cyclotron resonance mass spectrometry (FT-ICR MS) to overcome those problems and reveal that the most abundant species that comprise the largest aggregate segment are indeed the most aliphatic. The ability to characterize difficult-to-analyze samples, like asphaltenes, is the first major advantage of online coupling. Another benefit is the increased chromatographic resolution afforded by online coupling, which enables a finer examination in the most aggregated region and reveals a local trend opposed to the global trend. The very first species to elute in the largest aggregates were more condensed polyaromatic compounds, and the larger, more aliphatic species elute shortly thereafter in much greater relative abundance.

■ INTRODUCTION

Notoriously one of the most problematic components of crude oils—asphaltenes—can complicate every stage of the production chain.[1] On the recovery side, asphaltene deposition in pipelines can require production shutdowns to remove the blockage. On the refinery side, high asphaltene concentrations typically decrease a crude oil's yield and, simultaneously, increase maintenance costs. Asphaltenes are also possibly the most polydisperse and compositionally complex mixture in the world.[2−6] Unfortunately, asphaltenes are not a well-understood chemical compound class partly due to their poor definition: insolubility in an *n*-alkane solution, typically *n*-pentane or *n*-heptane.[7] Based on bulk properties, asphaltenes typically contain higher concentrations of polar heteroatoms and are more aromatic than their parent crude oils.[8−10] On the basis of these typical characteristics, it has long been believed that asphaltene nanoaggregation is driven primarily by $\pi-\pi$ stacking and hydrogen bonding between polar compounds. However, linking chemical functionalities to aggregation potential requires detailed molecular-level information, and the tendency of asphaltenes to aggregate results in very poor ionization efficiency and makes them extremely difficult to analyze.

Despite the challenges associated with the analysis of asphaltenes, recent work has begun to reveal that waxlike interactions between more aliphatic compounds may play a more important role in asphaltene aggregation than previously known. Berrueco et al. hypothesized that the earliest-eluting (most aggregated) molecular weight regime of gel permeation chromatography (GPC) fractions from asphaltenes, petroleum pitch, and coal-derived materials are composed of larger, more aliphatic compounds based on lower fluorescence and UV absorbance in this region.[11−13] GPC aggregate fractions collected from a typical atmospheric residue and characterized by positive-ion atmospheric pressure photoionization 9.4 T Fourier transform ion cyclotron resonance ((+)APPI) FT-ICR) mass spectrometry revealed aromaticity to vary inversely with aggregation potential.[14] The largest, most aggregated fractions were composed of large, very aliphatic compounds that ionize extremely poorly. In interfacially active asphaltenes (~2% subfraction that absorbs to the surface of water droplets), characterization by electrospray ionization mass

Received: June 29, 2020
Revised: August 3, 2020
Published: August 5, 2020

https://dx.doi.org/10.1021/acs.energyfuels.0c02158
Energy Fuels 2020, 34, 10915−10925

spectrometry (ESI-MS) and ^1H and ^{13}C nuclear magnetic resonance (NMR) spectroscopy revealed a larger molecular weight distribution in the interfacially active species compared to the whole asphaltenes. The interfacially active asphaltenes were also more aliphatic on average and enriched in sulfoxides compared to the whole asphaltenes.[15] In another study, it has also been shown that unstable asphaltenes have higher binding capacities for alkanes and waxes.[16] In fact, several recent studies have observed similar trends and reported GPC elution based on both mass and H/C ratio, with the more alkylated compounds eluting earliest.[17−19]

Gel permeation chromatography (GPC) can help probe the forces driving asphaltene aggregation by acting as a proxy for studying aggregation in a laboratory. GPC is often coupled online with detection by inductively coupled plasma mass spectrometry (ICP MS), thereby enabling the quantitative determination of individual elements. GPC ICP MS chromatograms are commonly termed size distributions or size profiles. Most commonly, sulfur is monitored along with the most abundant heavy metals in petroleum products (vanadium, nickel, and iron). Heavy metals are of interest due to their potential to deactivate hydrotreatment and hydrocracking catalysts during upgrading and refinery processes. Vanadium, nickel, and iron exist structurally in petroleum as porphyrins (heterocyclic macrocycles with four modified pyrrole subunits).[20,21] Metal-containing petroporphyrins are enriched in precipitated asphaltenes, but their exact role in asphaltene aggregation is unknown.[22] GPC ICP MS chromatograms for porphyrinic metals typically exhibit multimodal/trimodal aggregate size distributions that provide "fingerprints" for petroleum samples.[23,24] The determination of GPC aggregate size profiles can provide insight into specific refinery problems, and the method has been applied to saturates, aromatics, resins, and asphaltene fractions,[24,25] distillation cuts,[23] and isolated interfacial material.[26] However, it is not entirely clear how well GPC aggregation mimics "real-world" asphaltene aggregation in the field because elimination of possible surface effects during GPC separations is difficult, if not impossible.[27,28] GPC elution should be dictated entirely by hydrodynamic volume, and although that ideal may not be achievable, the appropriate choice of mobile phase and column conditions can help to ensure than hydrodynamic volume is the dominant elution mechanism.[13,29] To ensure that we do not infer too much from GPC results on their own, however, we shall discuss results with regard to aggregation tendencies observed during GPC elution.

In the analysis of complex mixtures, especially asphaltenes, ionization biases arise from differences in ionization efficiencies and aggregation tendencies, resulting in the preferential detection of the species that ionize most efficiently. Chromatographic separations help to overcome ionization biases by simplifying the sample matrix,[2,30] but just as important is the choice of ionization method. Positive-ion atmospheric pressure photoionization ((+)APPI) is widely thought to be the most compatible method for asphaltenes.[5,31,32] Despite the well-known ionization biases of aromatic compounds, APPI ionizes more uniformly compared to electrospray, which is why it was selected for this study,[5,33] which is the second installment of a study that investigates the aggregation tendencies and molecular composition of the PetroPhase 2017 asphaltene sample by use of GPC. In part 1, GPC aggregate fractions were collected from the PetroPhase 2017 asphaltene sample and analyzed by direct infusion.[34] Monomer ion yields and aggregation state were strongly correlated. The asphaltene fractions that were most aggregated ionized ~1000 times less efficiently than the least aggregated fractions in the whole crude oil. For all of the heteroatom classes observed in both the whole crude oil and the asphaltenes, the aggregate state and the relative abundance of larger, more alkylated species were closely correlated. The composition shifted toward more condensed polyaromatic species as aggregation decreased. The results from part 1 suggested that interactions between more aliphatic compounds may be a major contributor to aggregation. However, the extremely low monomer ion yields for these fractions limited our ability to characterize the asphaltenes by direct infusion to only a few of the most abundant heteroatom classes. By coupling the GPC separation with online detection by 21 T FT-ICR MS, this study overcomes some of the challenges and limitations encountered when asphaltene fractions were characterized by direct infusion. To further improve our ability to characterize the most aggregated regions of the GPC profile, which contains compounds with extremely poor ionization efficiencies, 4% (v/v) anisole was added to the postcolumn eluent to act as a dopant for detection by (+)APPI. Tetrahydrofuran (THF) on its own is compatible with (+)APPI, but anisole was added because it has been shown to be a very effective charge exchange dopant to improve ionization for compounds with low ionization efficiencies.[35] We did observe increased sensitivity in the largest aggregate region with the addition of anisole, and we hoped that it would translate to improved compositional coverage. The addition of anisole shifts the ionization process to favor the formation of radical cations; however, no significant differences in the number of species identified or the compositional coverage with anisole were observed.

Very few previous reports have combined chromatographic methods with online detection by FT-ICR MS to characterize petroleum products and/or asphaltenes.[36] Several close mass differences are critical to resolve in the analysis of petroleum products. Two particularly important mass differences are the 3.4 mDa (S_1H_4 vs C_3) and 1.1 mDa ($^{13}C_1H_3{}^{32}S_1$ vs C_4). These close mass differences make online detection by high-resolution MS difficult on a chromatographic time scale. Often, long transients are required to obtain high mass resolving power, and coaddition of time-domain transients is required to increase signal-to-noise ratio to maintain sufficient dynamic range. For that reason, many studies with online detection by high-resolution MS resemble fraction collection and analysis by direct infusion. One of the first studies that coupled a chromatographic separation with online detection by FT-ICR MS for the analysis of petroleum products divided the chromatogram into two main peaks.[37] Size exclusion chromatography has been coupled to ultrahigh-resolution MS to study asphaltenes only a handful of times. An early work by Ghislain et al. observed a ~50% higher number of molecular formulas assigned than by direct infusion, and despite the entire elution profile taking less than 5 min, they highlighted several examples of structural isomers that were resolved chromatographically.[17] One of the best examples by Guricaz et al. coupled size exclusion chromatography with a research-type LTQ-Orbitrap Elite mass spectrometer to study asphaltene aggregation.[38] The equivalent of six fractions was achieved through the coaddition of data acquisitions across 1 min periods. They also observed elution according to the H/C ratio. Compounds eluted according to the degree of alkylation;

the most aliphatic species eluted earliest, in the more aggregated regions.

EXPERIMENTAL SECTION

Instrumentation and Materials. For online FT-ICR MS, the GPC separation was performed with an Alliance e2695 separation module equipped with a WAT 005319 2 μm precolumn inline filter and a 2998 photodiode array (PDA). All Waters HPLC system components were operated with EMPOWER3 software (Waters Corporation, Milford, MA). The GPC column was a Varian PLgel (50 Å, 7.5 × 300 mm^2, 5 μm) HPLC column (Agilent Technologies, Santa Clara, CA). The flow rate was set to 0.20 mL/min with inhibitor-free HPLC grade (≥99.9%) tetrahydrofuran (THF) (Sigma-Aldrich, St. Louis, MO). Column components and detectors were connected with 0.020 in. stainless steel tubing (IDEX Health and Science LLC). When coupled with ICP MS, the GPC separation was performed with an AKTA purifier liquid chromatography system equipped with a UV-900 multiwavelength UV absorbance detector and a Frac-950 fraction collector (GE Healthcare Bio-Sciences, Pittsburgh, PA). For detection by ICP MS, most of the eluent was directed to waste by a postcolumn split, and ~40 μL/min was diverted to the detector (Thermo Scientific Element XRsector field ICP-HRMS). Differences in extracolumnar volumes between the experimental setup for detection with ICP-MS and 21 T FT-ICR MS were calculated theoretically to align the two chromatograms, and the elution times from a tetraphenyl porphyrin standard were monitored by UV−vis (prior to either postcolumn dilution/split); the porphyrin standard was detected by both ICP-MS and FT-ICR MS to verify that the elution times of the two systems were aligned. Experimental conditions for the ICP MS interface and detection have been described extensively in previous works.[14,23,24,39,40]

The APPI source (ThermoFisher Scientific, San Jose, CA) was set to a vaporization temperature of 350 °C, and N_2 was used for the sheath gas (50 psi) and the auxiliary gas (32 mL/min) to avoid sample oxidation. Experiments were performed with a custom-built hybrid dual ion-trap 21 T FT-ICR mass spectrometer described previously.[41,42] Excitation and detection were performed with a Predator data station.[43] Online detection by 21 T FT-ICR MS yields a mass resolving power of 3400000 at m/z 400 for an adsorption-mode mass spectrum (6.2 s transient duration), yielding 6451 unique assigned molecular formulas (120 ppb RMS error).[36] A 3.1 s transient often maximizes sensitivity and improves scan rate, while maintaining sufficient resolving power to separate the 1.1 mDa mass split out to ~m/z 700. In this study we expected to observe species with molecular weights as great as ~1000 Da, so we chose a 4.5 s transient to maintain resolution of the 1.1 mDa mass split. All spectra were phase-corrected for a mass resolving power of ~2500000 at m/z 400.[44] Predator Analysis and PetroOrg were used to perform mass calibration and to assign peaks.[45,46] For each individual mass spectrum, Excel spreadsheets containing relative abundances for all assigned heteroatom classes and groups were exported from PetroOrg. A custom-made python script was used to parse through and consolidate data from these Excel workbooks to generate extracted ion chromatograms (XICs) for individual heteroatom classes.

Purified Asphaltenes. Starting from an Arabian heavy crude oil provided by Total, asphaltenes were isolated by use of the standard ASTM D6560-12 method.[47] As previously reported,[48] four iterations of maceration followed by Soxhlet extraction with clean n-C_7 for 5 h (20 h total) was performed to further purify the asphaltenes and remove occluded material, which can account for up to 50 wt % of the initial asphaltenes.[49,50] The Arabian heavy purified asphaltenes (aka the PetroPhase 2017 Asphaltenes) were obtained as part of an international collaborative effort to study asphaltenes.[51] The same isolation and purification procedures were also performed for Athabasca Bitumen.

RESULTS AND DISCUSSION

GPC Chromatograms for Asphaltenes. The GPC separation of asphaltenes was performed in duplicate to utilize online detection by both ICP MS and 21 T FT-ICR MS. As shown in Figure 1, GPC ICP MS enables the quantitative determination of ^{32}S (blue) and ^{51}V (red) nanoaggregate size distributions. The size profiles exhibit typical asphaltene monomodal distributions that increase sharply on the peak front, are centered at ~28 min, and then decrease slowly on the tailing side until ~55 min. Most of the total sulfur and vanadium elute within the first 5 min of the total exclusion limit in the largest aggregate region (~25−30 min). Figure 1 also shows the (+)APPI total ion chromatogram (TIC) determined by 21 T FT-ICR MS in black. The TIC exhibits a more Gaussian-shaped broad peak that extends from ~25−55 min and is centered at ~36 min.

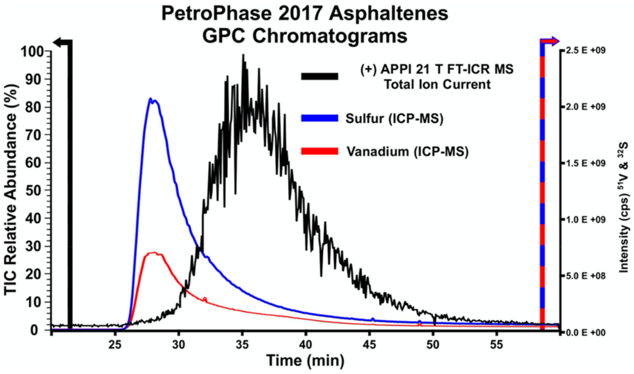

Figure 1. GPC total ion chromatogram (TIC) from (+)APPI 21 T FT-ICR mass spectral analysis of the PetroPhase 2017 asphaltenes plotted in black on the primary axis. Sulfur (blue) and vanadium (red) GPC ICP-MS chromatograms are plotted on the secondary axis on the right.

Figure 2 shows the TIC determined by FT-ICR MS (black) and the corresponding ^{51}V (red) GPC ICP-MS size profile for asphaltenes purified from Athabasca Bitumen. Both of these chromatograms resemble their counterparts from the PetroPhase 2017 asphaltene sample, but the bitumen asphaltenes have higher concentrations of heavy metals. Figure 2 also shows the FT-ICR MS extracted ion chromatogram (XIC) for

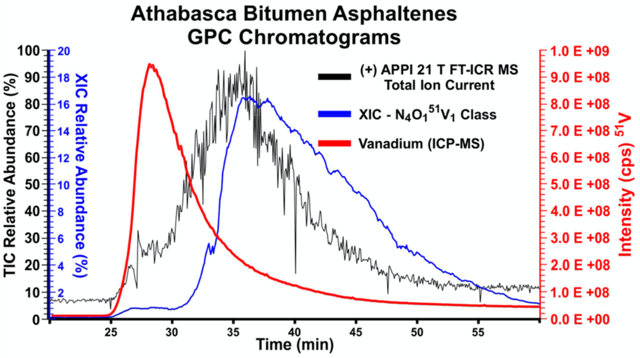

Figure 2. GPC TIC (black) and extracted ion chromatogram (XIC) for the $N_4O_1{}^{51}V_1$ heteroatom class (blue) from the (+)APPI mass spectral analysis of purified Athabasca Bitumen asphaltenes plotted on the left axes. The vanadium (red) GPC ICP-MS chromatogram is plotted on the secondary axis on the right.

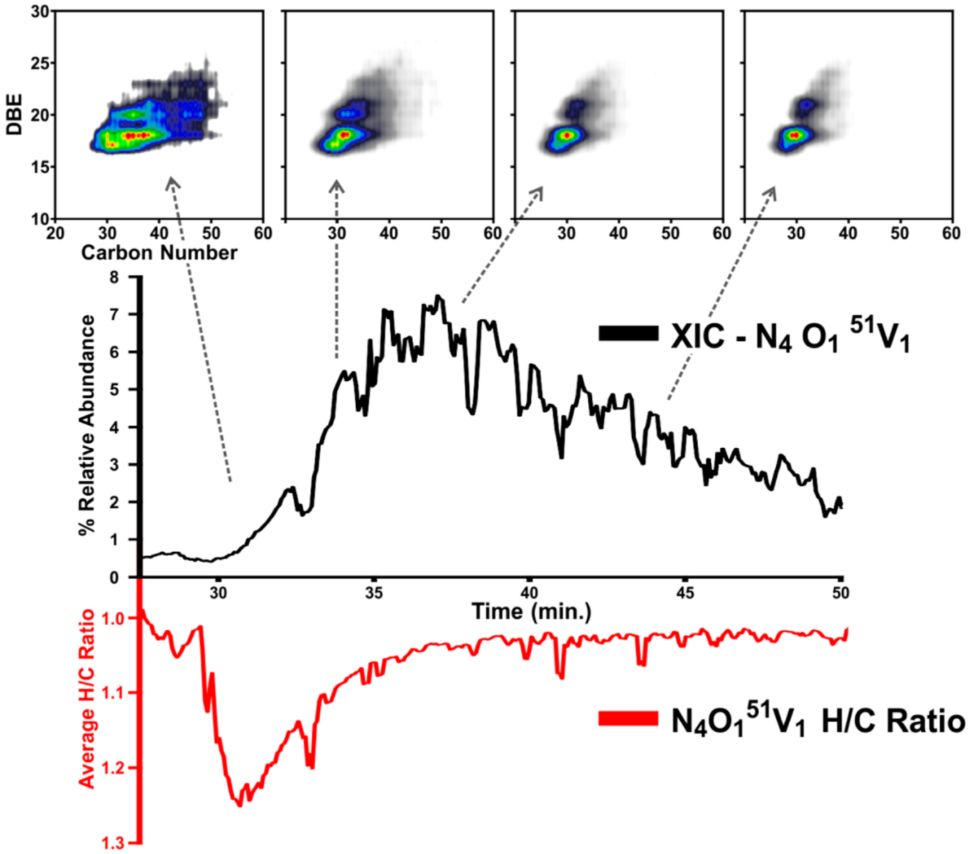

Figure 3. XIC and (+)APPI derived isoabundance color-contoured plots of double-bond equivalents (DBE) vs carbon number shown in order of elution from left to right for the $N_4O_1{}^{51}V_1$ heteroatom class (top) from the analysis of the PetroPhase 2017 asphaltenes. The inverted chromatogram shows the XIC's average H/C ratio (bottom).

the $N_4O_1{}^{51}V_1$ heteroatom class (blue) for comparison. Based on the total ^{52}V signal measured by ICP-MS, the vanadium content of the bitumen asphaltenes is ~1.5 times that of the PetroPhase 2017 asphaltenes. The higher concentration of vanadium makes the bitumen asphaltenes better suited to compare the chromatographic features of the mass profile (GPC ICP-MS) to those of the $N_4O_1{}^{51}V_1$ porphyrin heteroatom class (GPC FT-ICR MS). Approximately half of the total vanadium elutes in the most excluded region, from ~25−30 min; however, the XIC for the $N_4O_1{}^{51}V_1$ heteroatom class (the most abundant of the assigned vanadyl porphyrin classes) increases in relative abundance only slightly and plateaus at ~1% during the most aggregated elution period. The relative abundance begins to increase sharply at ~31 min, after more than half of the total vanadium has already eluted, and reaches its peak maximum of ~16% relative abundance at a time to that for the TIC at ~35 min. From the ~16-fold increase in relative abundance, combined with the ~5-fold decrease in GPC ICP-MS signal for ^{51}V during that time, we can infer qualitatively that the relative ionization efficiencies (aka monomer ion yield) of the vanadyl porphyrins eluting in the largest aggregates is ~80 times lower than those at ~36 min. The difference in monomer ion yield continues to increase with elution time and decreased aggregate size, consistent with previous results.

Online Detection Accesses the Compositional Changes of Asphaltene Species Not Observable by Direct Infusion. In our previous work, we analyzed GPC fractions collected from the same PetroPhase 2017 asphaltene sample by direct infusion with only moderate success. Chemical contaminants up-concentrated during the fraction collection and drying processes made the analysis of fractions collected with THF as the mobile phase impossible (even after several attempts), and results from runs with xylene as the mobile phase were limited to only the most abundant heteroatom classes (S_1, S_2, O_1S_1, and O_1S_2). Coupling the GPC separation with online detection eliminates the contaminant problem. Furthermore, because the dynamic range increases quadratically with magnetic field strength, detection by 21 T FT-ICR MS helped overcome the dynamic range limitations encountered at lower fields. The dynamic range is especially important for difficult-to-analyze samples with low ionization efficiencies (i.e., asphaltenes and their GPC fractions).

With online detection by 21 T FT-ICR MS we can also extract more detailed molecular information than just a heteroatom class relative abundances and gain more insight into why the earliest eluting porphyrins ionize so poorly. For example, Figure 3 shows the XIC for the $N_4O_1{}^{51}V_1$ porphyrin heteroatom class from the PetroPhase 2017 asphaltenes in black. The same XIC is also plotted with the abundance-weighted average H/C ratio as the *y*-axis instead of relative abundance. The average H/C ratio XIC is shown in red with the *y*-axis inverted, and it gives us a measure of aromaticity for the $N_4O_1{}^{51}V_1$ porphyrin heteroatom class.[52] The aromaticity and H/C ratio are inversely related, so the earliest eluting porphyrins are least aromatic, as confirmed by the (+)APPI derived isoabundance color-contoured plots of double-bond

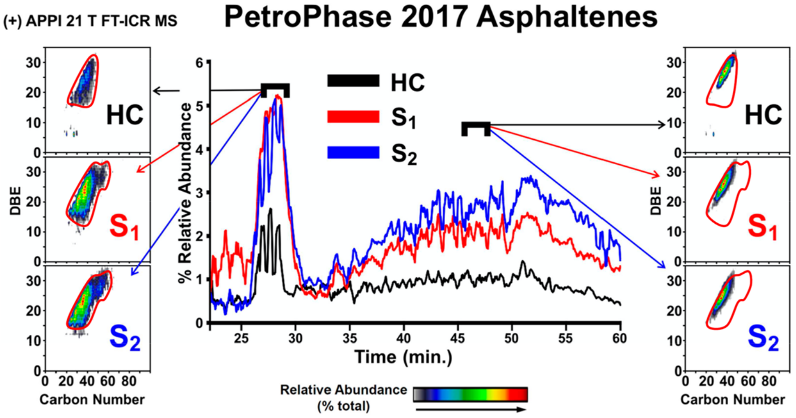

Figure 4. GPC FT-ICR MS extracted ion chromatograms for the hydrocarbon and sulfur heteroatom classes (center). Positive APPI-derived isoabundance contour plots of DBE vs carbon number for the HC class (top), S_1 class (middle), and S_2 class (bottom) with short retention times (left) and long retention times (right). As aggregation decreases, the compositional range for each class moves from more aliphatic species on the left toward condensed polycyclic aromatics on the right.

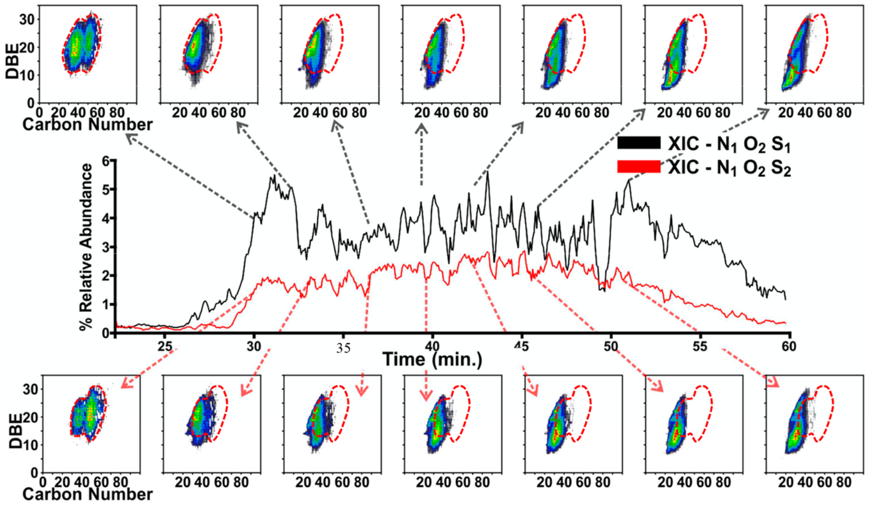

Figure 5. Extracted ion chromatograms and plots of DBE vs carbon number shown in order of elution from left to right for the $N_1O_2S_1$ (top) and $N_1O_2S_2$ (bottom) heteroatom classes from the PetroPhase 2017 asphaltenes. As aggregation decreases, the compositional range shifts toward more condensed aromatics in the high DBE range, and the abundance of lower DBE species increases, possibly indicating a shift in structural motifs (i.e., from thiophenic to sulfidic sulfur).

equivalents vs carbon number for the $N_4O_1{}^{51}V_1$ class (Figure 3, top). The composition of the vanadyl porphyrins eluting in the most aggregated region (leftmost plot) spans the largest carbon number range. As aggregation lessens, the carbon number range narrows and the average H/C ratio decreases to almost 1.0, corresponding to species with very little alkylation on the core, tetrapyrrolic porphyrin structure.[24,53,54] Increased aggregation correlated to decreased aromaticity and greater abundance of more aliphatic species for all of the heteroatom classes observed. Figure 4 confirms that correlation for three of the most abundant heteroatom classes in the whole asphaltenes. GPC FT-ICR MS XICs for the HC, S_1, and S_2 heteroatom classes are shown in black, red, and blue. Plots of carbon number vs DBE for early eluting (left) and later-eluting (right) regions have the distribution for the most aggregated elution period circled in red for comparison. The earliest, most aggregated region spans the widest carbon number range, and as aggregation decreases, the compositional range for all three heteroatom classes moves from more aliphatic species on the left toward condensed polycyclic aromatics on the right.

For the PetroPhase 2017 asphaltene sample, we were able to successfully characterize the S_x heteroatom classes by direct infusion; however, we were not able to obtain molecular information for polyheteroatomic classes, such as $N_xO_yS_z$, in the high molecular weight fraction even after multiple attempts. Online detection grants access to these heteroatom classes by eliminating the need to blow down large volumes of solvents to dry fractions, thereby up-concentrating chemical contaminants. Figure 5 shows the XIC and composition for the $N_1O_2S_1$ and $N_1O_2S_2$ heteroatom classes. The red outlines correspond to the composition of the earliest-eluting species in the largest aggregates. As aggregation decreases, two main trends are apparent. First, in the high DBE range, alkylation decreases, and the composition shifts toward more condensed aromatics. Second, a distribution of lower DBE species emerges as aggregation continues to decrease, which likely indicating a change in the sulfur moiety, possibly from thiophenic (aromatic) to sulfidic (aliphatic) sulfur.

Observations in composition of the O_1S_1, O_1S_2, and O_2S_1 heteroatom classes support the inference that a change in

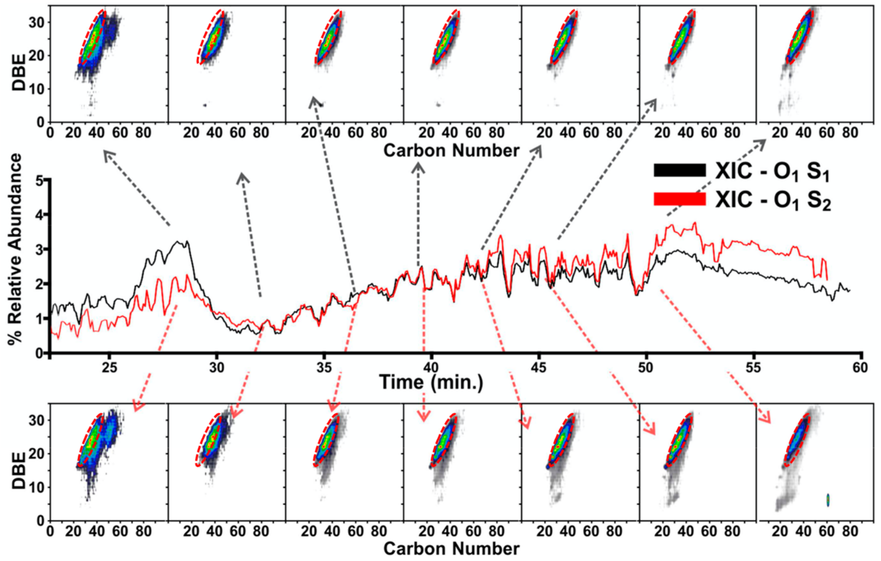

Figure 6. Extracted ion chromatograms and plots of DBE vs carbon number shown in order of elution from left to right for the O_1S_1 (top) and O_1S_2 (bottom) heteroatom classes from the PetroPhase 2017 asphaltenes.

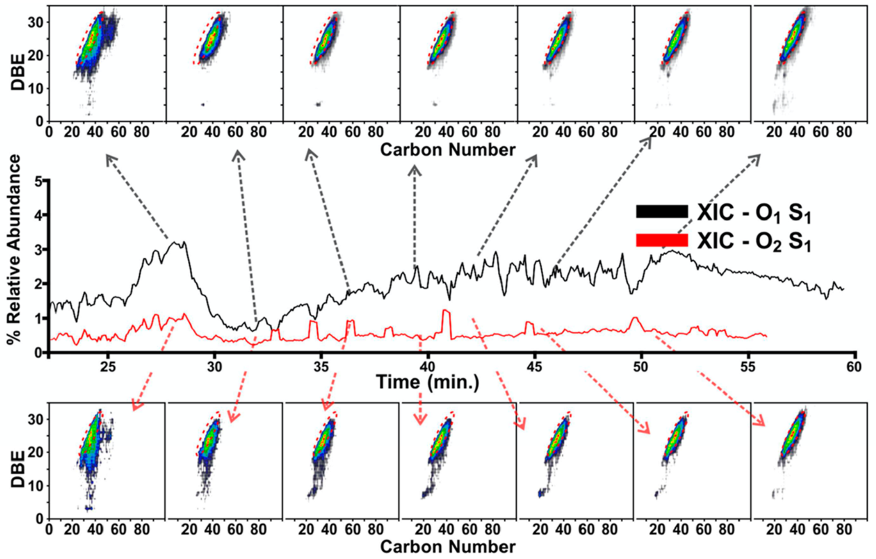

Figure 7. Extracted ion chromatograms and plots of DBE vs carbon number shown in order of elution from left to right for the O_1S_1 (top) and O_2S_1 (bottom) heteroatom classes from the PetroPhase 2017 asphaltenes.

sulfur moieties is likely responsible for the appearance of the second, lower-DBE species in the less aggregated region. Figures 6 and 7 show extracted ion chromatograms and track the composition of those three heteroatom classes. To compare changes with the incorporation of a single oxygen vs a single sulfur heteroatom, both figures show the O_1S_1 XIC in black with the corresponding DBE vs carbon number plots on the top. In black and on the bottom, Figure 6 shows the XIC and composition of the O_1S_2 heteroatom class, whereas Figure 7 shows the XIC and composition of the O_2S_1 heteroatom class. Plots are shown in order of elution from left to right, and the dotted red ovals represent the composition of species that elute latest, in the nonaggregated region. For all three heteroatom classes, the most abundant species in the high DBE region are near the polyaromatic hydrocarbon planar limit and correspond to condensed aromatic compounds with very little alkylation.[55] As aggregate size increases, the degree of alkylation gradually increases. In the largest aggregates, both the O_1S_1 and O_1S_2 heteroatom classes exhibit a bimodal distribution with a second distribution between DBE ∼25−30 and ∼45−60 carbons. There are also a few species in low abundance with DBE < ∼15 that elute with the largest aggregates before ∼30 min for both classes. In the O_1S_1 heteroatom class, compounds with DBE < 15 are absent until the latest elution period at ∼50 min, but in the O_1S_2 class, low DBE species appear again in low abundance at ∼35 min. These species become more numerous, gradually increasing in relative abundance and decreasing in DBE with increasing elution time. The region that elutes last contains the peaks corresponding to species with DBE < 15 for any of the elution regions. Compared to the O_1S_2 class, the opposite trend is observed in the composition of the O_2S_1 heteroatom class in the low-DBE region. As shown in the bottom of Figure 7, the earliest eluting region with the largest

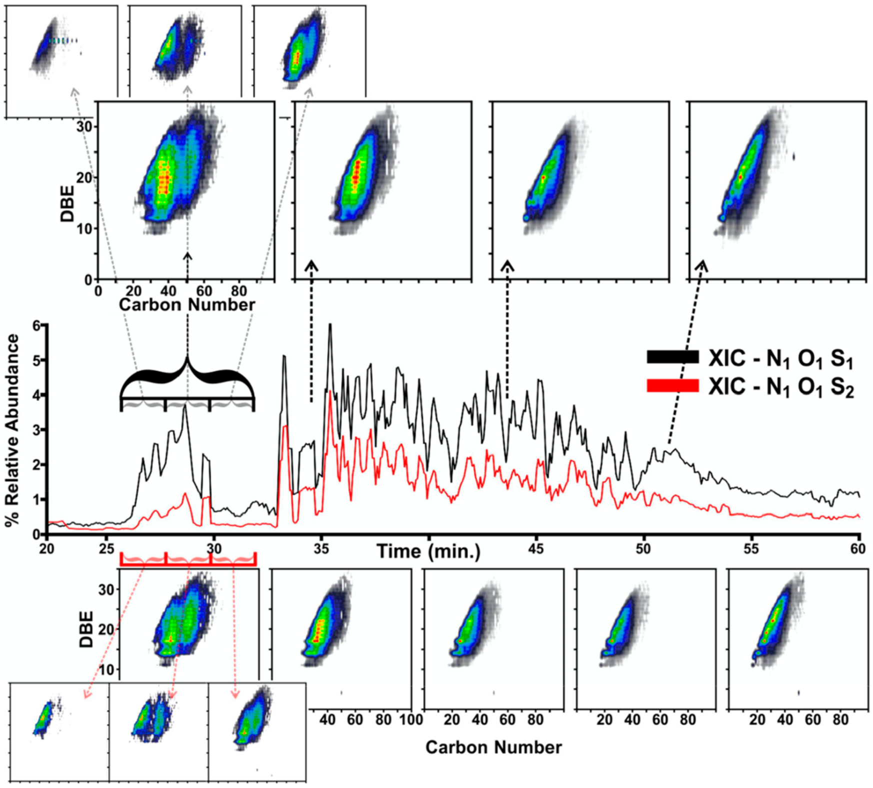

Figure 8. Extracted ion chromatograms and plots of DBE vs carbon number for the PetroPhase 2017 asphaltenes shown in order of elution from left to right for the $N_1O_1S_1$ (top) and $N_1O_1S_2$ (bottom) heteroatom classes. The composition for the most aggregated species exhibits a bimodal distribution. Online detection enables the small overlaid plots to show three discrete segments of that region. The shorter time windows reveal that the first species to elute are actually more aromatic, with DBE ≈ 20−25. Those species are followed closely by more alkylated compounds in much higher relative abundance.

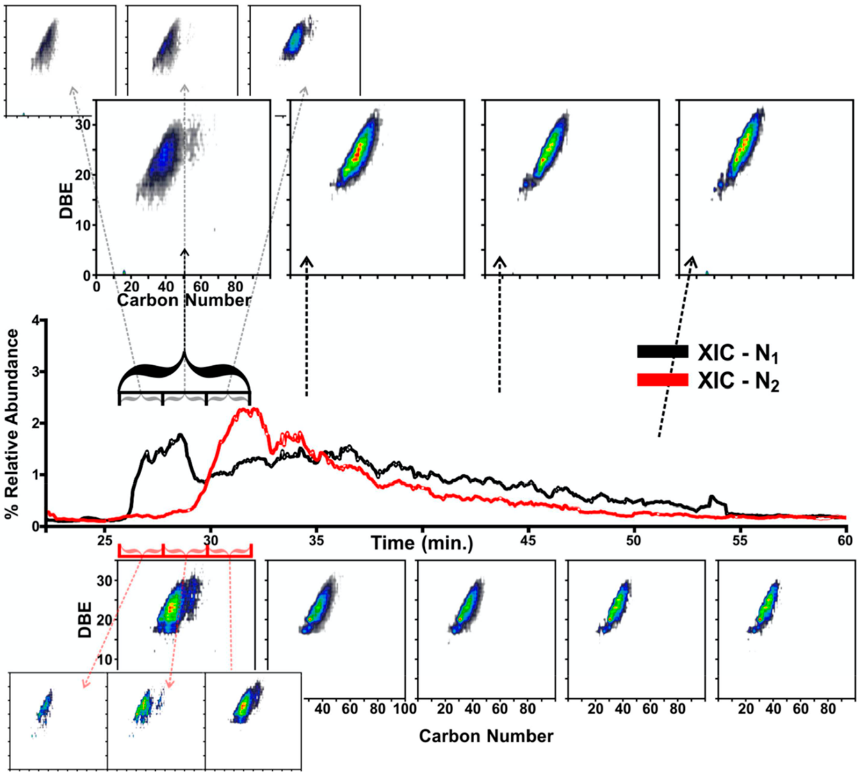

Figure 9. Extracted ion chromatograms and plots of DBE vs carbon number for the PetroPhase 2017 asphaltenes shown in order of elution from left to right for the N_1 (top) and N_2 (bottom) heteroatom classes.

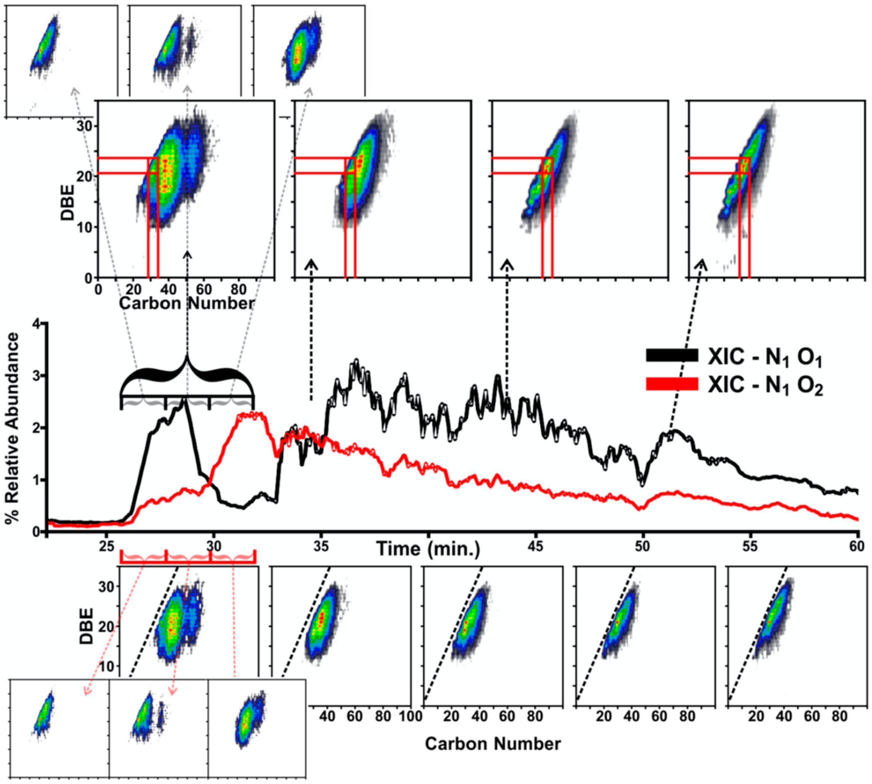

Figure 10. Extracted ion chromatograms and plots of DBE vs carbon number for the PetroPhase 2017 asphaltenes shown in order of elution from left to right for the N_1O_1 (top) and N_1O_2 (bottom) heteroatom classes.

aggregates contains the greatest number of O_2S_1 species with DBE less than 15. As elution time increases, low-DBE O_2S_1 species decrease in number and in relative abundance. On the far right, in the least-aggregated region, only a few O_2S_1 species are observed in extremely low relative abundance.

Improved Chromatographic Resolution with Online Detection Reveals Local Trends That Oppose the Global Trends. The first major advantage with online detection is the ability to track compositional changes for heteroatom classes not observable by direct infusion, making it well suited for analysis of samples with low ionization efficiencies. The second major advantage is the increased chromatographic resolution afforded by online detection. For the $N_1O_1S_1$ and $N_1O_1S_2$ heteroatom classes shown in Figure 8, we observe the same global trends as previously discussed. The XICs for the $N_1O_1S_1$ (black) and $N_1O_1S_2$ (red) heteroatom exhibit a bimodal distribution with a smaller, narrow peak eluting near the total exclusion limit from ~25−30 min and a second, broader, later-eluting hump from ~34−55 min. The isoabundance-contoured plots of DBE vs carbon number on the top correspond to the $N_1O_1S_1$ class, whereas those on the bottom correspond to the $N_1O_1S_2$ heteroatom class. The plots of DBE vs carbon number directly above and below the XICs show the composition of large elution periods of ~7 min. The longer elution periods reveal the same global trends discussed previously at length. If we were able to successfully track compositional changes for those heteroatom classes by direct infusion (which we were not able to do), we would expect to observe similar global trends. The most aliphatic species elute earliest in the largest aggregates, and aromaticity increases as aggregation lessens at longer elution times. However, the composition of the most aggregated species exhibits a bimodal distribution. Online detection enables the small overlaid plots to reveal three discrete segments of that region. The shorter time windows reveal that the first species to elute are actually more aromatic, with DBE ~ 20−25. Those species are followed closely by more alkylated compounds in much higher relative abundance. Globally, the most aliphatic species elute first in the largest aggregates, but locally, within that region the trend is the opposite. In addition to improving our ability to extract information for difficult-to-analyze samples, the increased chromatographic resolution reveals local trends in most-aggregated region that oppose the global trend for both the $N_1O_1S_1$ and $N_1O_1S_2$ heteroatom classes.

The local trend in the largest aggregates was not limited to polyheteroatomic classes with many polar functional groups. We observed the same local trend in the most aggregated region for all the heteroatom classes we examined. Figure 9 shows the N_1 and N_2 heteroatom classes XICs in black/red and composition on the top/bottom. The XIC for the N_1 heteroatom class reaches its maximum relative abundance of ~2% at ~27 min. Note that the N_2 heteroatom class is offset by ~4 min and stays closer to baseline level during that elution period. At ~30 min, its relative abundance begins to increase, finally reaching its maximum value of just over 2% relative abundance at ~31 min. Globally, the earliest elution window for both heteroatom classes spans the widest carbon number range, and as elution increases and aggregation decreases, the composition shifts toward condensed polyaromatics with very little alkylation. However, locally, within the earliest, most-aggregated elution window, the trend is the opposite. The very first compounds to elute at ~26 min are more aromatic, and by 28 min, the composition has shifted to more aliphatic species with longer alkyl chains in greater abundance.

Consistent with the prior discussion, similar trends are observed in the composition of the N_1O_1 and N_1O_2 heteroatom classes, shown in Figure 10. The nonaggregated region is composed of species that correspond to condensed polyaromatic cores, with only short alkyl substitutions. The solid red lines within the carbon number vs DBE plots on the top highlight the most abundant species in the least-aggregated region that elutes last. For the N_1O_1 heteroatom class, these hot spots are located between DBE ∼21−24 and carbon numbers ∼29−35. In the plots on the bottom that show the composition of the N_1O_2 heteroatom class, the black dashed lines represent the theoretical polyaromatic hydrocarbon limit, or PAH line, and provide an alternative way to compare the changes in aromaticity as a function of aggregate state. In the smallest aggregates, the composition is within ∼10 carbons of the PAH line. For both heteroatom classes, as aggregate size increases moving to the left, alkylation increases, and the composition shifts away from the PAH line, and alkylation increases. In the largest aggregate region, species are observed ∼40 carbons away from the PAH limit and 60 total carbons in both the N_1O_1 and N_1O_2 heteroatom classes. These species correspond to extremely aliphatic compounds with long alkyl substitutions on the aromatic cores. The compositional range covered by both heteroatom classes exhibits a similar bimodal distribution observed in the most aggregated regions of the $N_xO_yS_z$ and O_xS_y heteroatom classes, and once again, the improved chromatographic resolution afforded by online detection reveals a local trend opposite that of the global trend in this region. The very earliest compounds that elute are actually closer to the PAH limit and are more aromatic. Those species are quickly followed by more alkylated compounds in greater relative abundance.

■ CONCLUSIONS

GPC coupled with online detection successfully overcomes the challenges associated with fraction collection and analysis by direct infusion and reveals that for all heteroatom classes in the PetroPhase 2017 asphaltene sample aggregate size and aromaticity are inversely correlated. The largest aggregate region is composed of the most alkylated species, and the composition shifts toward more aromatic compounds as aggregation decreases. In addition to the ability to characterize samples with extremely low ionization efficiencies, online coupling improves the chromatographic resolution, which enables a closer examination of the most aggregated region. Smaller time segments revealed a local trend in the largest aggregates that opposed the global trend. The very first species to elute in the largest aggregates are actually more aromatic, and more alkylated compounds eluted shortly thereafter in greater relative abundance. Even disregarding the limitations associated with fraction collection and direct infusion, it would be difficult (and certainly impractical) to collect a sufficient number of fractions with short enough time intervals to reveal this local trend in the largest aggregates.

■ AUTHOR INFORMATION

Corresponding Authors

Alan G. Marshall − *National High Magnetic Field Laboratory and Department of Chemistry and Biochemistry, Florida State University, Tallahassee, Florida 32310, United States;* orcid.org/0000-0001-9375-2532; Phone: 1-850-644-0529; Email: marshall@magnet.fsu.edu; Fax: 1-850-644-1366

Brice Bouyssière − *International Joint Laboratory−iC2MC: Complex Matrices Molecular Characterization, TRTG, 76700 Harfleur, France; TOTAL Raffinage Chimie, TRTG, 76700 Harfleur, France; E2S UPPA, CNRS, IPREM, Institut des Sciences Analytiques et de Physico-chimie pour l'Environnement et les Materiaux, UMR5254, Hélioparc, Universite de Pau et des Pays de l'Adour, 64053 Pau, France;* orcid.org/0000-0001-5878-6067; Phone: +33 (0) 559 407 752; Email: brice.bouyssiere@univ-pau.fr; Fax: +33 (0) 559 407 781

Authors

Jonathan C. Putman − *National High Magnetic Field Laboratory and Department of Chemistry and Biochemistry, Florida State University, Tallahassee, Florida 32310, United States; Exum Instruments, Denver, Colorado 80223, United States*

Rémi Moulian − *International Joint Laboratory−iC2MC: Complex Matrices Molecular Characterization, TRTG, 76700 Harfleur, France; TOTAL Raffinage Chimie, TRTG, 76700 Harfleur, France; E2S UPPA, CNRS, IPREM, Institut des Sciences Analytiques et de Physico-chimie pour l'Environnement et les Materiaux, UMR5254, Hélioparc, Universite de Pau et des Pays de l'Adour, 64053 Pau, France*

Donald F. Smith − *National High Magnetic Field Laboratory, Florida State University, Tallahassee, Florida 32310, United States;* orcid.org/0000-0003-3331-0526

Chad R. Weisbrod − *National High Magnetic Field Laboratory, Florida State University, Tallahassee, Florida 32310, United States;* orcid.org/0000-0001-5324-4525

Martha L. Chacón-Patiño − *National High Magnetic Field Laboratory, Florida State University, Tallahassee, Florida 32310, United States;* orcid.org/0000-0002-7273-5343

Yuri E. Corilo − *National High Magnetic Field Laboratory, Florida State University, Tallahassee, Florida 32310, United States*

Greg T. Blakney − *National High Magnetic Field Laboratory, Florida State University, Tallahassee, Florida 32310, United States;* orcid.org/0000-0002-4205-9866

Leah E. Rumancik − *Department of Computer Science, Florida State University, Tallahassee, Florida 32304, United States*

Caroline Barrère-Mangote − *International Joint Laboratory−iC2MC: Complex Matrices Molecular Characterization, TRTG, 76700 Harfleur, France; TOTAL Raffinage Chimie, TRTG, 76700 Harfleur, France*

Ryan P. Rodgers − *National High Magnetic Field Laboratory, Department of Chemistry and Biochemistry, and Future Fuels Institute, Florida State University, Tallahassee, Florida 32310, United States; International Joint Laboratory−iC2MC: Complex Matrices Molecular Characterization, TRTG, 76700 Harfleur, France; E2S UPPA, CNRS, IPREM, Institut des Sciences Analytiques et de Physico-chimie pour l'Environnement et les Materiaux, UMR5254, Hélioparc, Universite de Pau et des Pays de l'Adour, 64053 Pau, France;* orcid.org/0000-0003-1302-2850

Pierre Giusti − *International Joint Laboratory−iC2MC: Complex Matrices Molecular Characterization, TRTG, 76700 Harfleur, France; TOTAL Raffinage Chimie, TRTG, 76700 Harfleur, France;* orcid.org/0000-0002-9569-3158

Complete contact information is available at:
https://pubs.acs.org/10.1021/acs.energyfuels.0c02158

Notes

The authors declare no competing financial interest.

■ ACKNOWLEDGMENTS

This work was supported by the National Science Foundation Division of Chemistry through Cooperative Agreements No. DMR-11-57490 and DMR-1644779, the State of Florida, Conseil Régional d'Aquitaine (20071303002PFM), and FEDER (31486/08011464). The authors thank TOTAL for supplying oil samples and Steven M. Rowland for helpful discussions and feedback.

■ REFERENCES

(1) Akbarzadeh, K.; Hammami, A.; Kharrat, A.; Zhang, D.; Allenson, S.; Creek, J.; Kabir, S.; Jamaluddin, A.; Marshall, A. G.; Rodgers, R. P.; Mullins, O. C.; Solbakken, T. *Oilf. Rev.* **2007**, *19* (2), 22−43.

(2) Chacón-Patiño, M. L.; Rowland, S. M.; Rodgers, R. P. *Energy Fuels* **2018**, *32* (1), 314−328.

(3) Herod, A. A. *Rapid Commun. Mass Spectrom.* **2010**, *24* (17), 2507−2519.

(4) Herod, A. A.; Bartle, K. D.; Morgan, T. J.; Kandiyoti, R. *Chem. Rev.* **2012**, *112* (7), 3892−3923.

(5) McKenna, A. M.; Marshall, A. G.; Rodgers, R. P. *Energy Fuels* **2013**, *27* (3), 1257−1267.

(6) Purcell, J. M.; Merdrignac, I.; Rodgers, R. P.; Marshall, A. G.; Gauthier, T.; Guibard, I. *Energy Fuels* **2010**, *24*, 2257−2265.

(7) Fan, T.; Buckley, J. S. *Energy Fuels* **2002**, *16* (6), 1571−1575.

(8) Miller, J. T.; Fisher, R. B.; Thiyagarajan, P.; Winans, R. E.; Hunt, J. E. *Energy Fuels* **1998**, *12* (6), 1290−1298.

(9) Rogel, E.; Roye, M.; Vien, J.; Miao, T. *Energy Fuels* **2015**, *29* (4), 2143−2152.

(10) Buenrostro-Gonzalez, E.; Groenzin, H.; Lira-Galeana, C.; Mullins, O. C. *Energy Fuels* **2001**, *15* (4), 972−978.

(11) Hansen, B. E.; Malmros, O.; Turner, N. R.; Stenby, E. H.; Andersen, S. I. In *Proceedings of Light Metals*; New Orleans, LA, 2001; pp 559−564.

(12) Lazaro, M. J.; Islas, C. A.; Herod, A. A.; Kandiyoti, R. *Energy Fuels* **1999**, *13* (6), 1212−1222.

(13) Berrueco, C.; Venditti, S.; Morgan, T. J.; Álvarez, P.; Millan, M.; Herod, A. A.; Kandiyoti, R. *Energy Fuels* **2008**, *22* (5), 3265−3274.

(14) Putman, J. C.; Gutiérrez Sama, S.; Barrère-Mangote, C.; Rodgers, R. P.; Lobinski, R.; Marshall, A. G.; Bouyssieere, B.; Giusti, P. *Energy Fuels* **2018**, *32*, 12198.

(15) Qiao, P.; Harbottle, D.; Tchoukov, P.; Masliyah, J.; Sjoblom, J.; Liu, Q.; Xu, Z. *Energy Fuels* **2017**, *31*, 3330−3337.

(16) Orea, M.; Ranaudo, M. A.; Lugo, P.; López, L. *Energy Fuels* **2016**, *30* (10), 8098−8113.

(17) Ghislain, T.; Molnárné Guricza, L.; Schrader, W. *Rapid Commun. Mass Spectrom.* **2017**, *31* (6), 495−502.

(18) Panda, S. K.; Alawani, N. A.; Lajami, A. R.; Al-Qunaysi, T. A.; Muller, H. *Fuel* **2019**, *235*, 1420−1426.

(19) Alawani, N. A.; Panda, S. K.; Lajami, A. R.; Al-Qunaysi, T. A.; Muller, H. *Energy Fuels* **2020**, *34*, 5414.

(20) Xu, H.; Que, G.; Yu, D.; Lu, J. *Energy Fuels* **2005**, *19* (6), 517−524.

(21) López, L.; Lo Mónaco, S.; Richardson, M. *Org. Geochem.* **1998**, *29*, 613−629.

(22) Gascon, G.; Vargas, V.; Feo, L.; Castellano, O.; Castillo, J.; Giusti, P.; Acavedo, S.; Lienemann, C. P.; Bouyssiere, B. *Energy Fuels* **2017**, *31* (8), 7783−7788.

(23) Desprez, A.; Bouyssiere, B.; Arnaudguilhem, C.; Krier, G.; Vernex-loset, L.; Giusti, P. *Energy Fuels* **2014**, *26*, 3730−3737.

(24) Gutierrez Sama, S.; Desprez, A.; Krier, G.; Lienemann, C.-P.; Barbier, J. J.; Lobinski, R.; Barrere-Mangote, C.; Giusti, P.; Bouyssiere, B. *Energy Fuels* **2016**, *30* (9), 6907−6912.

(25) Cui, Q.; Nakabayashi, K.; Ma, X.; Miyawaki, J.; Al-mutairi, A.; Mj, A.; Park, J.; Yoon, S.; Mochida, I. *Energy Fuels* **2017**, *31* (7), 6637.

(26) Ligiero, L. M.; Bouriat, P.; Dicharry, C.; Passade-Boupat, N.; Lalli, P. M.; Rodgers, R. P.; Barrère-Mangote, C.; Giusti, P.; Bouyssiere, B. *Energy Fuels* **2017**, *31* (2), 1065−1071.

(27) Sato, S.; Takanohashi, T.; Tanaka, R. *Energy Fuels* **2005**, *19* (5), 1991−1994.

(28) Prokai, L.; Simonsick, W. J., Jr. *Rapid Commun. Mass Spectrom.* **1993**, *7* (9), 853−856.

(29) Lathe, G. H.; Ruthven, C. R. J. *Biochem. J.* **1956**, *62* (4), 665−674.

(30) Rowland, S. M.; Robbins, W. K.; Corilo, Y. E.; Marshall, A. G.; Rodgers, R. P. *Energy Fuels* **2014**, *28* (8), 5043−5048.

(31) Itoh, N.; Aoyagi, Y.; Yarita, T. *J. Chromatogr. A* **2006**, *1131* (1−2), 285−288.

(32) Robb, D. B.; Covey, T. R.; Bruins, a. P. *Anal. Chem.* **2000**, *72* (15), 3653−3659.

(33) Andreatta, G.; Bostrom, N.; Mullins, O. C. *Langmuir* **2005**, *21* (7), 2728−2736.

(34) Putman, J. C.; Moulian, R.; Barrère-Mangote, C.; Rodgers, R. P.; Bouyssiere, B.; Giusti, P.; Marshall, A. G. *Energy Fuels* **2020**, *34*, 8308.

(35) Smith, D. R.; Robb, D. B.; Blades, M. W. *J. Am. Soc. Mass Spectrom.* **2009**, *20*, 73−79.

(36) Putman, J. C.; Smith, D. F.; Weisbrod, C. R.; Rowland, S. M.; Patiño, M. L. C.; Corilo, Y. E.; Blakney, G. T.; Hendrickson, C. L.; Rodgers, R. P.; Marshall, A. G. In *Proceedings of the 67th ASMS Conference on Mass Spectrometry and Allied Topics*, 2019.

(37) Lababidi, S.; Schrader, W. *Rapid Commun. Mass Spectrom.* **2014**, *28* (12), 1345−1352.

(38) Molnárné Guricza, L.; Schrader, W. *Fuel* **2018**, *215*, 631−637.

(39) Giusti, P.; Nuevo Ordonez, Y.; Philippe Lienemann, C.; Schaumloffel, D.; Bouyssiere, B.; Lobinski, R. *J. Anal. At. Spectrom.* **2007**, *22* (1), 88−92.

(40) Caumette, G.; Lienemann, C.-P.; Merdrignac, I.; Paucot, H.; Bouyssiere, B.; Lobinski, R. *Talanta* **2009**, *80* (2), 1039−1043.

(41) Hendrickson, C. L.; Quinn, J. P.; Kaiser, N. K.; Smith, D. F.; Blakney, G. T.; Chen, T.; Marshall, A. G.; Weisbrod, C. R.; Beu, S. C. *J. Am. Soc. Mass Spectrom.* **2015**, *26* (9), 1626−1632.

(42) Smith, D. F.; Podgorski, D. C.; Rodgers, R. P.; Blakney, G. T.; Hendrickson, C. L. *Anal. Chem.* **2018**, *90* (3), 2041−2047.

(43) Blakney, G. T.; Hendrickson, C. L.; Marshall, A. G. *Int. J. Mass Spectrom.* **2011**, *306* (2−3), 246−252.

(44) Xian, F.; Hendrickson, C. L.; Blakney, G. T.; Beu, S. C.; Marshall, A. G. *Anal. Chem.* **2010**, *82* (21), 8807−8812.

(45) Blakney, G. T.; Hendrickson, C. L.; Marshall, A. G. *Int. J. Mass Spectrom.* **2011**, *306* (2−3), 246−252.

(46) Corilo, Y. E. *PetroOrg. Software*; Florida State University: Tallahassee, FL, 2017.

(47) ASTM D6560. Standard Test Method for Determination of Asphaltenes (Heptane Insolubles) in Crude Petroleum and Petroleum Products; ASTM International: West Conshohocken, PA, 2017; www.astm.org.

(48) Chacón-Patiño, M. L.; Vesga-Martínez, S. J.; Blanco-Tirado, C.; Orrego-Ruiz, J. A.; Gómez-Escudero, A.; Combariza, M. Y. *Energy Fuels* **2016**, *30* (6), 4550−4561.

(49) Derakhshesh, M.; Bergmann, A.; Gray, M. R. *Energy Fuels* **2013**, *27* (4), 1748−1751.

(50) Strausz, O. P.; Torres, M.; Lown, E. M.; Safarik, I.; Murgich, J. *Energy Fuels* **2006**, *20* (5), 2013−2021.

(51) Giusti, P.; Bouyssieere, B.; Carrier, H.; Afonso, C. *Energy Fuels* **2018**, *32*, 2641.

(52) Santos Silva, H.; Sodero, A. C. R.; Korb, J. P.; Alfarra, A.; Giusti, P.; Vallverdu, G.; Bégué, D.; Baraille, I.; Bouyssiere, B. *Fuel* **2017**, *188*, 374−381.

(53) Santos Silva, H.; Sodero, A. C. R.; Korb, J. P.; Alfarra, A.; Giusti, P.; Vallverdu, G.; Bégué, D.; Baraille, I.; Bouyssiere, B. *Fuel* **2017**, *188*, 374−381.

(54) Santos Silva, H.; Alfarra, A.; Vallverdu, G.; Bégué, D.; Bouyssiere, B.; Baraille, I. *Pet. Sci.* **2020**, *17* (3), 797−810.

(55) Hsu, C. S.; Lobodin, V. V.; Rodgers, R. P.; McKenna, A. M.; Marshall, A. G. *Energy Fuels* **2011**, 25 (5), 2174−2178.